Electric quadrupole moments of the 2_1^+ states in ^{100,102,104}Cd

A. Ekström,[1] J. Cederkäll,[1,2] D. D. DiJulio,[1] C. Fahlander,[1] M. Hjorth-Jensen,[3] A. Blazhev,[4] B. Bruyneel,[4] P. A. Butler,[5] T. Davinson,[6] J. Eberth,[4] C. Fransen,[4] K. Geibel,[4] H. Hess,[4] O. Ivanov,[7] J. Iwanicki,[8] O. Kester,[9] J. Kownacki,[8] U. Köster,[2,10] B. A. Marsh,[11,12] P. Reiter,[4] M. Scheck,[5] B. Siebeck,[4] S. Siem,[13] I. Stefanescu,[7] H. K. Toft,[13] G. M. Tveten,[2,13] J. Van de Walle,[2] D. Voulot,[12] N. Warr,[4] D. Weisshaar,[4] F. Wenander,[12] K. Wrzosek,[8] and M. Zielińska[8,14]

[1]*Physics Department, University of Lund, Box 118, SE-221 00 Lund, Sweden*
[2]*PH Department, CERN 1211, Geneva 23, Switzerland*
[3]*Physics Department and Center of Mathematics for Applications, University of Oslo, Norway*
[4]*Institute of Nuclear Physics, University of Cologne, Germany*
[5]*Oliver Lodge Laboratory, University of Liverpool, United Kingdom*
[6]*Department of Physics and Astronomy, University of Edinburgh, United Kingdom*
[7]*Instituut voor Kern- en Stralingsfysica, K. U. Leuven, Celestijnenlaan 200D B-3001, Belgium*
[8]*Heavy Ion Laboratory, University of Warsaw, Poland*
[9]*Gesellschaft für Schwerionenforschung, Darmstadt, Germany*
[10]*Institut Laue Langevin, 6 rue Jules Horowitz, F-38042 Grenoble, France*
[11]*Department of Physics, University of Manchester, United Kingdom*
[12]*AB Department, CERN 1211, Geneva 23, Switzerland*
[13]*Department of Physics, University of Oslo, Norway*
[14]*CEA Saclay, Service de Physique Nucléaire, Gif-sur-Yvette, France*

(Received 20 May 2009; revised manuscript received 5 October 2009; published 3 November 2009)

Using the REX-ISOLDE facility at CERN the Coulomb excitation cross sections for the $0_{gs}^+ \rightarrow 2_1^+$ transition in the β-unstable isotopes ^{100,102,104}Cd have been measured for the first time. Two different targets were used, which allows for the first extraction of the static electric quadrupole moments $Q(2_1^+)$ in ^{102,104}Cd. In addition to the $B(E2)$ values in ^{102,104}Cd, a first experimental limit for the $B(E2)$ value in ^{100}Cd is presented. The data was analyzed using the maximum likelihood method. The provided probability distributions impose a test for theoretical predictions of the static and dynamic moments. The data are interpreted within the shell-model using realistic matrix elements obtained from a G-matrix renormalized CD-Bonn interaction. In view of recent results for the light Sn isotopes the data are discussed in the context of a renormalization of the neutron effective charge. This study is the first to use the reorientation effect for post-accelerated short-lived radioactive isotopes to simultaneously determine the $B(E2)$ and the $Q(2_1^+)$ values.

DOI: 10.1103/PhysRevC.80.054302 PACS number(s): 23.20.Js, 21.60.Cs, 25.70.De, 27.60.+j

I. INTRODUCTION

The isotopes ^{100}Cd, ^{102}Cd, and ^{104}Cd belong to a region of the Segrè chart where excited states at low energy evolve from being governed by single-particle effects to be dominated by collective motion. The gradual alignment of the angular momentum vectors of the two proton holes in ^{98}Cd [1,2] describes the principal part of its wave function up the first 8^+ state. In contrast, vibrational and rotational behavior develop in the surrounding isotopes. At $N \sim 60$ the Cd isotopes are weakly deformed with $\beta_2 \sim 0.1$ [3] and exhibit a low-energy structure of vibrational character [4,5] manifested by a $0_2^+, 2_2^+, 4_1^+$ triplet at nearly twice the energy of the 2_1^+ state. As a consequence, several previous studies of the Cd isotopes [6–10] have focused on interpretations within a multiphonon picture with excitations of quadrupole and quadrupole-octupole type.

Theoretically, the spectra of $^{98-106}$Cd have been described in the spherical shell model and in a variety of interacting boson models [11,12]. In a recent series of measurements several groups [13–16] report reduced excitation probabilities for the $0_{gs}^+ \rightarrow 2_1^+$ transition in ^{106,108,110}Sn, which deviate from predictions based on realistic effective nucleon-nucleon interactions. The observed $B(E2)$ discrepancy in the light Sn isotopes appears to originate from an incomplete description of the residual nucleon-nucleon interaction outside the ^{100}Sn core. As a complement to a study of the interaction as a function of the neutron degree of freedom, the neutron-deficient Cd isotopes lend themselves to a similar study where the proton degree of freedom is invoked as well. This aspect is the principal motivation for the work presented here. We also present the results from shell-model calculations based on a realistic effective interaction.

In general, the reduced transition probability for electromagnetic de-excitations between nuclear states is a very sensitive probe of the nuclear wave function. The lifetimes of the low-lying states in ^{102,104}Cd were recently visited employing a plunger device in a recoil distance Doppler-shift (RDDS) measurement, see Refs. [17,18]. In sub-barrier Coulomb excitation the 2_1^+ state can be populated via a direct transition from the ground state, circumventing issues related to feeding through higher lying states. However, the extracted $B(E2)$ value is connected to the sign and magnitude of

the static quadrupole moment $Q(2_1^+)$ via the total Coulomb excitation cross section. Therefore, this study and the lifetime-based investigations are complementary.

In this article we present the results from the first sub-barrier Coulomb excitation measurements of the $0_{gs}^+ \rightarrow 2_1^+$ cross section in ^{100,102,104}Cd. From these measurements the $B(E2; 0_{gs}^+ \rightarrow 2_1^+)$ value in ^{100,102,104}Cd was determined and the $Q(2_1^+)$ in ^{102,104}Cd was extracted using the reorientation effect [19,20]. The technique of combined cross-section measurements was explored for the first time using a short-lived radioactive ion beam thus providing a test of the intensity limit for this method for future radioactive beam measurements.

II. RADIOACTIVE ION BEAM PRODUCTION AND DETECTOR EQUIPMENT

The first excited state in ^{100,102,104}Cd was populated by bombarding the respective Cd isotope onto target foils of either 1.8 mg/cm^2 ^{64}Zn or 1.9 mg/cm^2 ^{109}Ag. The experiment was carried out at the ISOLDE facility at CERN. The methods of production, postacceleration, and data collection are similar to that of Ref. [21]. The radioactive ion beams were produced by impinging a 1.4 GeV proton beam delivered by the CERN PS-Booster on a 27 g/cm^2-thick LaC_x target. The Cd atoms were ionized using a resonant laser ionization scheme providing Cd^+ ions for subsequent electrostatic extraction. The isotope mass was selected using the high-resolution separator of the facility. Contaminating In isobars were suppressed using a primary target with a temperature controlled quartz transfer line [22]. Due to the different vapor pressures of In and Cd at the chosen target temperature a relative reduction of the contaminant of two orders of magnitude was reached. The intensity of the contaminant was determined from the number of elastically scattered particles at the secondary target during laser on/off measurements [15,16,21]. Postacceleration in the REX-LINAC requires a mass-to-charge ratio less than 4.5 that was fulfilled after approximately 62 ms of charge breeding in the REX-EBIS [23]. At the final beam energy of 2.87 MeV/u the scattering occurs below the Coulomb barrier for any combination of projectiles and targets used here [19].

Ejectiles and recoils were detected by a circular double-sided silicon strip detector (DSSSD) placed 32.5 mm downstream of the secondary target covering laboratory angles $\theta \in [15^\circ, 52^\circ]$. The 16 annular strips covering each quadrant of the detector have a pitch per strip of 1.9 mm, whereas, for the current experiment, the 24 radial strips were coupled pairwise, resulting in a 6.8° radial pitch. For further details see Ref. [24]. The γ rays were detected by the Miniball detector array that comprised 21 sixfold segmented germanium crystals at the time of the experiment. The absolute efficiency was 6% at a γ-ray energy of 1 MeV. Data collection was triggered by a particle-γ coincidence condition. An overview of the experimental parameters is given in Table I. The magnitude of the isobaric contamination of the ^{100}Cd beam was found to be consistent with zero within an experimental uncertainty of less than 10%. The upper limit is motivated by the systematics of the other measurements shown in Table I and by similar measurements in Refs. [15,16]. The intensity of the Cd beams fell with decreasing mass of the isotope. This in combination with the increasing excitation energy of the 2_1^+ state and the expected decrease of the corresponding $B(E2)$ value required longer measuring times for isotopes closer to the proton drip line.

III. EVENT STRUCTURE AND DATA REDUCTION

Time-coincident particle-γ data were collected with an 800 ns coincidence window. A pure particle trigger, downscaled by a factor of 64 to reduce the amount of surplus data and acquisition dead time, was used outside of this gate. Prompt coincidences were selected offline using a 125 ns gate in the particle-γ time spectrum; see Fig. 1. The γ-ray detection efficiency was increased (10% gain at $E_\gamma = 1$ MeV) by using an offline add-back scheme [15,16]. The angular position of the germanium detectors was fine tuned in the offline analysis with the condition of minimizing the full width at half maximum (FWHM) of the Doppler corrected peaks. The DSSSD was energy calibrated based on the known target thickness and theoretical energy loss curves calculated by SRIM [25]. Assuming the particle interaction point to be in the center of the target resulted in a good Doppler correction of the detected γ rays. The physics events stored on disk are of two types: (i) a 1p event, which is ejectile *or* recoil detected, and (ii) a 2p event, which is ejectile *and* recoil detected.

A discussion related to the 2p and 1p event structure in REX-ISOLDE experiments can be found in Refs. [15,16,26]. In brief, the probability that the ejectile and the recoil simultaneously scatter into a given annular range of the DSSSD is limited by kinematics and by the distance between the secondary target and the DSSSD. A 2p event is constructed when two particles are detected in diametrically opposite quadrants within 100 ns. A 1p event occurs when one of

TABLE I. The experimental parameters for each of the measurements in this work. The measurements were carried out in the order they appear below. It should be noted that the ^{104}Cd beam intensity had to be reduced to avoid damage to the particle detector.

Beam	Target	Beam energy (MeV)	Beam intensity (pps)	Isobaric contamination (%)
^{104}Cd	^{109}Ag	298.5	1×10^6	0.8 ± 0.1
^{102}Cd	^{109}Ag	292.7	5×10^5	0.4 ± 0.1
^{102}Cd	^{64}Zn	292.7	5×10^4	2.7 ± 0.3
^{104}Cd	^{64}Zn	298.5	6×10^5	0.4 ± 0.1
^{100}Cd	^{109}Ag	287.0	3×10^3	0.0 ± 10.0

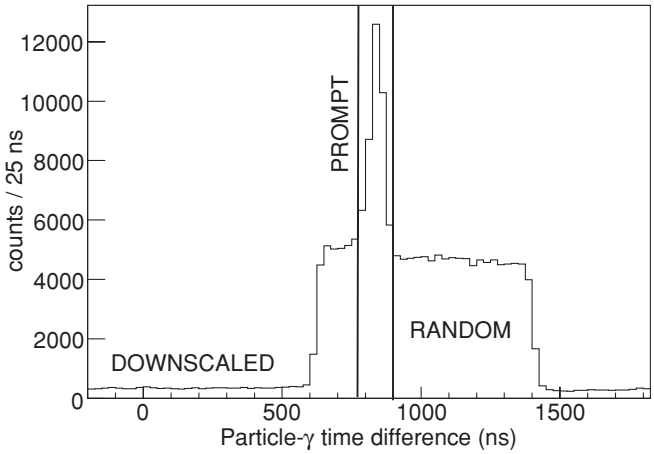

FIG. 1. Particle-γ time-difference spectrum. The prompt particle-γ coincidence window is indicated with vertical lines.

the particles either scatters outside of the annular range of the detector or when it penetrates the DSSSD undetected due to dead-time effects. Given the two-body kinematics of the scattering process, the missing particle in a 1p event can be reconstructed.

IV. DATA ANALYSIS

The spin and parity sequence of the first two excited states in ^{100,102,104}Cd are given in Fig. 2. The $2_1^+ \rightarrow 0_{gs}^+$ transitions treated in this work have energies of 1004, 777, and 658 keV, respectively. A reorientation measurement of the reduced transition probability and the static quadrupole moment requires at least two measurements under different conditions. This was accomplished here by adopting two different target materials, ^{64}Zn and ^{109}Ag, as well as different angular ranges for detection. In ^{64}Zn the 2_1^+ state is located 991 keV above the 0^+ ground state. The 2_2^+ state at 1799 keV is at a too-high energy to be visible in the data under the current experimental conditions. The ^{109}Ag nucleus exhibits a more complicated level structure; see Fig. 2. The $(\frac{5}{2}^-)_1 \rightarrow (\frac{1}{2}^-)_{gs}$ and $(\frac{3}{1}^-)_1 \rightarrow (\frac{1}{2}^-)_{gs}$ transitions at 415 and 311 keV were observed in the present data set. A summary of the $E2$ matrix elements for the ^{64}Zn target is given in Table II and similarly for the ^{109}Ag target in Table III. For an extended discussion of the adopted values see below. The experimentally determined γ-ray yields are presented in Table IV. In the following sections the method used in the analysis is expanded on followed by the specific results for different measurements.

TABLE II. The level index, spin, parity, level energy, and reduced matrix elements $\langle i||E2||j\rangle = M_{ij}$, in units of e b, for ^{64}Zn, used in the analysis Refs. [27–30].

Level	I^π	Energy (MeV)	1	2	3
1	0^+	0	0.0	0.400(19)	0.043(2)
2	2^+	0.991		−0.420(79)[a]	0.545(28)
3	2^+	1.799			0.0

[a]Positive $M_{12}M_{23}M_{13}$ interference value.

A. Method

1. The Coulomb excitation cross section

The $0_{gs}^+ \rightarrow 2_1^+$ Coulomb excitation cross section is given by

$$\sigma_{E2} = \sigma_R[\kappa_1(\theta_{c.m.}, \xi)B(E2)(1 + \kappa_2(\theta_{c.m.}, \xi)Q(2_1^+))] \quad (1)$$

in second-order perturbation theory. It depends on the Rutherford cross section, σ_R, the reduced transition probability,

$$B(E2; 0_{gs}^+ \rightarrow 2_1^+) = |\langle 0_{gs}^+||E2||2_1^+\rangle|^2 \equiv M_{12}^2, \quad (2)$$

and the spectroscopic quadrupole moment,

$$Q(2_1^+) = \frac{4}{5}\sqrt{\frac{2\pi}{7}}\langle 2_1^+||E2||2_1^+\rangle \equiv 0.75793 M_{22}. \quad (3)$$

The product of the $B(E2)$ and $Q(2_1^+)$ terms describes the reorientation effect. The positive definite coefficients κ_1 and κ_2 are known from perturbation theory [19] and depend on the center-of-mass scattering angle, $\theta_{c.m.}$, and the adiabaticity parameter, ξ. Generally, this dependence leads to an increase in the excitation cross section with increasing beam energy, atomic number, and scattering angle. However, at small $\theta_{c.m.}$, the cross section becomes less sensitive to the sign and magnitude of the static moment. For the ^{104}Cd and ^{102}Cd measurements relative to the ^{64}Zn target the statistics made it possible to extract the cross section also for very small scattering angles, i.e., corresponding to the first two or three of the innermost annular strips of the DSSSD. This provides a third set of data in addition to the ^{109}Ag data and the ^{64}Zn data measured at larger scattering angles.

As mentioned above, lifetime data exist for the 2_1^+ state in ^{104,102}Cd [18,30]. The $B(E2)$ value is, however, still not well established as the number of measurements remains small. The approach adopted here provides two options. The measurements for the two targets can be used independently of previous lifetime measurements to extract a new $B(E2)$ value and a static moment, or the measurements can be combined with previous lifetime measurements to improve the accuracy of the static moment, $Q(2_1^+)$, see e.g., Ref. [33]. We present results using both these approaches.

The projectile excitation cross section, σ^P, is determined by normalization against the corresponding known cross section for a given target, σ^T. The introduction of the two measured γ-ray yields for projectile and target, N_γ^P and N_γ^T, gives;

$$\sigma^P(B, Q) = \frac{N_\gamma^P}{N_\gamma^T}\frac{\varepsilon_\gamma^T}{\varepsilon_\gamma^P}\frac{W(\theta)^T}{W(\theta)^P}\frac{1}{1-q}\sigma^T. \quad (4)$$

In practice this procedure provides a measure of the incoming beam intensity. The relative γ-ray detection efficiencies, ε_γ, were obtained using a known ^{152}Eu calibration source. $W(\theta)$ represents the integrated angular distribution of de-excitation γ rays and q represents the fraction of isobaric contamination present in the beam. The cross sections were calculated using the computer code CLX [34] and included effects of energy loss in the target.

TABLE III. The level index, spin, parity, level energy, and reduced matrix elements $\langle i||E2||j\rangle = M_{ij}$, in units of e b, for ^{109}Ag, used in the analysis Refs. [30–32].

Level	I^π	Energy (MeV)	1	2	3	4	5	6
1	$\frac{1}{2}^-$	0.0	0.0	0.0	0.0	0.666(27)	0.800(33)	0.042(5)
2	$\frac{7}{2}^+$	0.088		0.0	3.046(15)	0.0	0.0	0.0
3	$\frac{9}{2}^+$	0.133			0.0	0.0	0.0	0.0
4	$\frac{3}{2}^-$	0.311				−0.905(388)	0.219(112)	0.0
5	$\frac{5}{2}^-$	0.415					−0.423(423)	0.0
6	$\frac{3}{2}^-$	0.702						0.0

2. *The maximum likelihood estimator*

The projectile matrix elements $\langle 0^+_{gs}||E2||2^+_1\rangle$ and $\langle 2^+_1||E2||2^+_1\rangle$ are extracted using a maximum likelihood approach. This method has the advantage that all data are treated on an equal footing and are weighted only by their uncertainties. The likelihood, $\mathcal{L}$, is a function of the nuclear parameters $B(E2)$ and $Q(2^+_1)$. It is defined as a product of probability distributions, P_k, one for each measurement.

$$\mathcal{L}(B, Q) = \prod_{k\in[Zn,Ag,\tau]} P_k(B, Q). \tag{5}$$

In the numerical analysis, P_k is approximated by a Gaussian probability distribution along the gradient of the contour curve of the k-th measurement. The statistical errors in the γ-ray yield measurements and the known uncertainties in the target matrix elements can be propagated to give the uncertainty in the total cross section. The standard deviation of the cross section in turn provides a 1-σ band in the $B(E2) - Q(2^+_1)$ plane. In short, the likelihood function for the Cd isotope of interest represents the total probability of (B, Q) being the pair of parameters that best reproduces the experimental projectile cross sections and the lifetime $\tau(2^+_1)$. The $\mathcal{L}$ is evaluated for $B \in [0, 1]e^2\,\mathrm{b}^2$ and $Q \in [-2, 2]\,e\,\mathrm{b}$. This corresponds to static and dynamic quadrupole moments that are in line with existing data in the Cd isotopic chain. The final $B(E2)$ and $Q(2^+_1)$ values, $\hat{B}$ and $\hat{Q}$, maximize the normalized likelihood function, i.e., $\mathcal{L}(\hat{B}, \hat{Q}) = 1.0$. The corresponding uncertainties are extracted from the contour curve $\mathcal{L}(B, Q) = 0.682$ projected on the respective axis.

TABLE IV. Experimental γ-ray yields as extracted from the data analysis.

Measurement	Transition	γ-ray yield
^{104}Cd + ^{64}Zn		
	^{104}Cd: $2^+_1 \to 0^+_{gs}$	1487(59)
	^{64}Zn: $2^+_1 \to 0^+_{gs}$	471(28)
^{104}Cd + ^{109}Ag		
	^{104}Cd: $2^+_1 \to 0^+_{gs}$	1028(47)
	^{109}Ag: $\frac{3}{2}^-_1 \to \frac{1}{2}^-_{gs}$	2753(95)
	^{109}Ag: $\frac{5}{2}^-_1 \to \frac{1}{2}^-_{gs}$	2289(84)
^{102}Cd + ^{64}Zn		
	^{102}Cd: $2^+_1 \to 0^+_{gs}$	308(28)
	^{64}Zn: $2^+_1 \to 0^+_{gs}$	156(23)
^{102}Cd + ^{109}Ag		
	^{102}Cd: $2^+_1 \to 0^+_{gs}$	486(34)
	^{109}Ag: $\frac{3}{2}^-_1 \to \frac{1}{2}^-_{gs}$	2249(83)
	^{109}Ag: $\frac{5}{2}^-_1 \to \frac{1}{2}^-_{gs}$	1985(65)
^{100}Cd + ^{109}Ag		
	^{100}Cd: $2^+_1 \to 0^+_{gs}$	$\leqslant$6.0(24)
	^{109}Ag: $\frac{3}{2}^-_1 \to \frac{1}{2}^-_{gs}$	101(17)
	^{109}Ag: $\frac{5}{2}^-_1 \to \frac{1}{2}^-_{gs}$	75(14)

B. γ-ray yields and transitions

1. ^{102,104}Cd *measurements*

With the ^{64}Zn target it is possible to identify the scattered projectile and target nuclei directly; see Fig. 3. Typical Doppler corrected γ-ray spectra, for the ^{102}Cd + ^{64}Zn case, are shown in Fig. 4. The satellite peak next to the $2^+_1 \to 0^+_{gs}$ target transition comes from two γ-ray transitions at 1025.0 and 1036.6 keV in the ^{102}Cd $\to$ ^{102}Ag $\to$ ^{102}Pd decay chain. Exactly the same satellite peak is present in the data from the ^{104}Cd + ^{64}Zn measurement and is due to remnant radioactive ^{102}Cd isotopes in the target chamber. The analyses of the ^{104}Cd + ^{109}Ag and ^{102}Cd + ^{109}Ag measurements are more elaborate. Given the approximately equal masses of these nuclei the kinematic distributions of the scattered particles overlap as can be seen in Fig. 3. This in turn eliminates the possibility of direct particle identification. As an example, simulations using the Rutherford cross section, σ_R, for the ^{104}Cd case show that 97% of the particles scattered into the DSSSD are ^{104}Cd nuclei. Thus a significant number of ^{109}Ag γ rays will be Doppler corrected using the experimental kinematics of a detected ^{104}Cd nucleus. Correspondingly, Doppler correcting all experimental 1p events using the respective masses gives the γ-ray spectra shown in Figs. 5(a) and 5(b). The broad structure present at the bottom part of the Doppler corrected γ-ray peaks arises from the effect mentioned above. The magnitude of this pedestal is proportional to the number of target γ rays detected in coincidence with scattered beam nuclei and vice versa. This effect was analyzed further by simulating the Coulomb excitation cross section $\sigma_{E2} = \sigma_R \cdot P(\theta)$, where

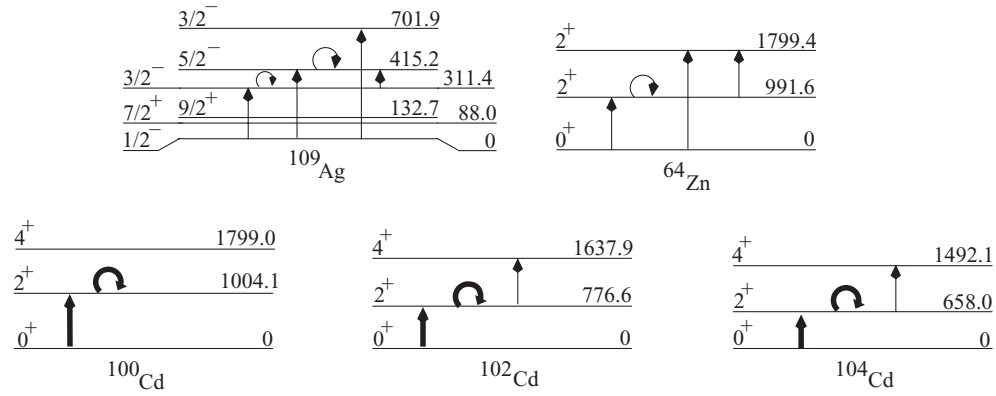

FIG. 2. Experimental level schemes for the projectile and the target isotopes. The relevant diagonal and nondiagonal $E2$ transitions are indicated with arrows. Transitions marked with a bold arrow are fitted in the analysis.

$P(\theta)$ is the known Coulomb excitation probability [19] for the ^{109}Ag target nuclei. The following effects were taken into account in the simulation: the energy loss of the particles as they traversed the target foil, the adiabaticity parameter ξ, the angular distributions $W(\theta)$, the Doppler shift of emitted γ rays, the experimental γ-ray detection efficiency, and the exact DSSSD geometry. Furthermore, a Gaussian distributed beam spot with a standard deviation of 1 mm was used. The simulated γ-ray energy spectrum is shown in Fig. 5(c). The simulation agrees with the experimental data. In detail, the γ rays from the 415 keV $(\frac{5}{2})_1^- \rightarrow (\frac{1}{2})_{gs}^-$ transition are registered in coincidence with a projectile particle in 76%

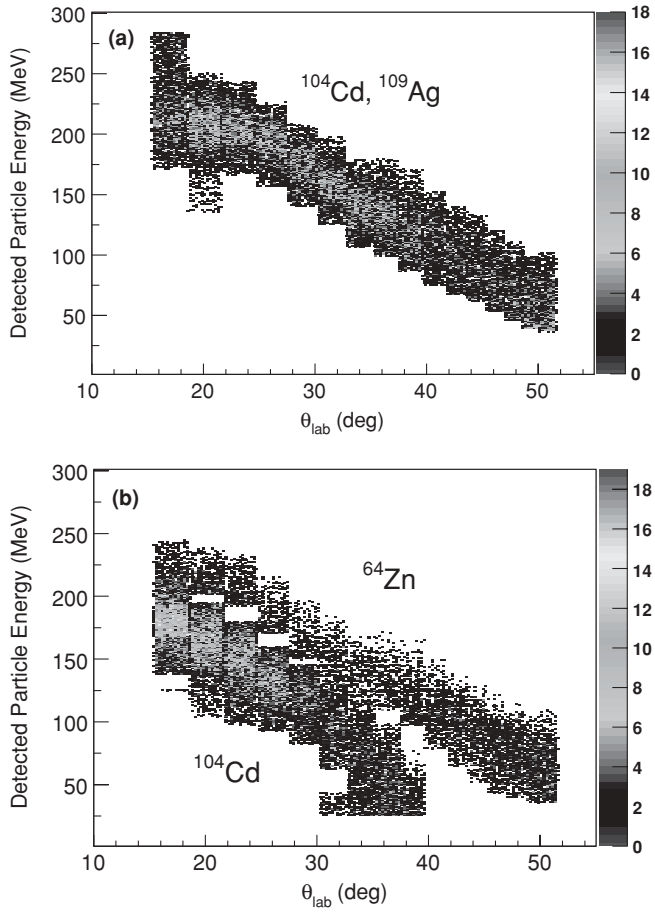

FIG. 3. Energy versus angle of the scattered beam and target particles detected by the DSSSD in the (a) ^{104}Cd + ^{109}Ag measurement and (b) ^{104}Cd + ^{64}Zn measurement.

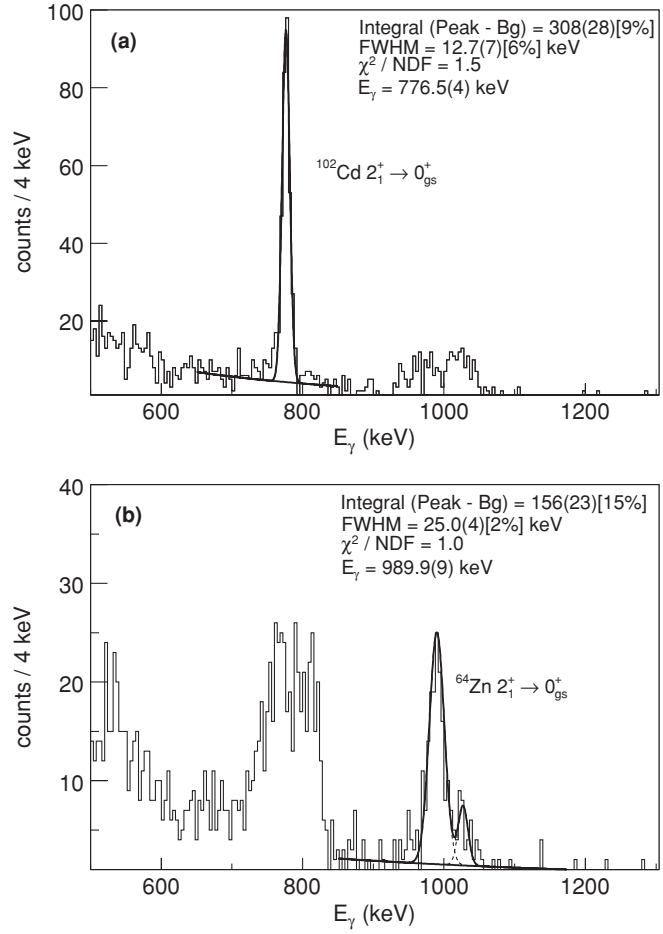

FIG. 4. The Doppler corrected γ-ray energy spectra from the ^{102}Cd + ^{64}Zn measurement. (a) The ^{102}Cd projectile de-excitation peak and (b) the ^{64}Zn target de-excitation peak.

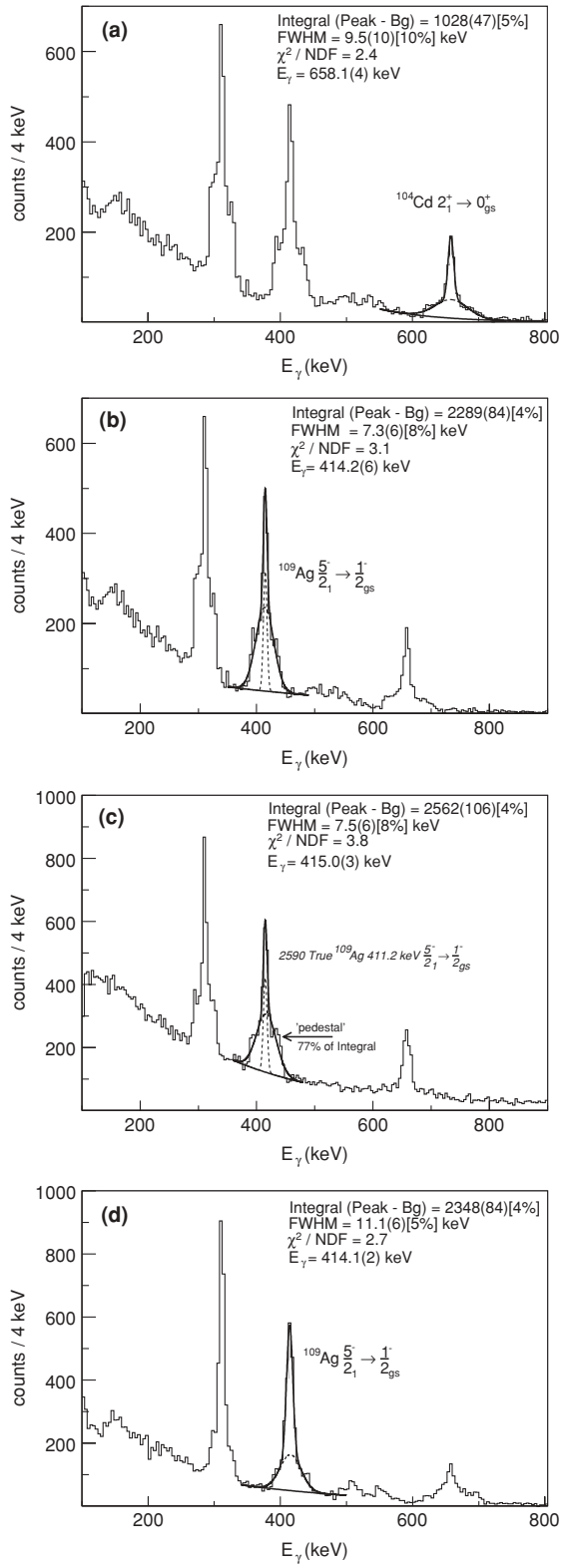

FIG. 5. [(a) and (b)] The Doppler-corrected γ-ray energy spectra from the ^{104}Cd + ^{109}Ag measurement. The pedestal comes from the ambiguity in the particle identification process. (c) Monte Carlo simulation of the effects of incomplete particle identification in the Doppler correction process. (d) Doppler-corrected γ rays from the ^{109}Ag target using the reconstructed momentum vectors of these particles.

of the Monte Carlo events. According to the fit in Fig. 5(c), the size of the corresponding simulated pedestal is 77(5)%. The experimental pedestal is 78(4)%. Furthermore, it can be verified that the total number of events estimated by the fit routine is accurate within one standard deviation.

Turning to the experimental data set again, it is possible to Doppler correct the transitions in ^{109}Ag using reconstructed momentum vectors of these particles. As expected, this reduces the pedestal of the corresponding peaks, see Fig. 5(d). However, note that the integrated γ-ray yields remain unchanged within one standard deviation. The reconstructed data thus shows consistency but was not used further in the analysis.

2. *The* ^{100}Cd + ^{109}Ag *measurement*

Within the time constraint of the experiment, a few ^{100}Cd events were detected. In this measurement the ^{109}Ag target was chosen over the ^{64}Zn target due to the higher Z of the former. As mentioned, the particle count rate in the DSSSD vanished when the laser ionization was switched off. The Doppler corrected spectrum, Fig. 6, is virtually free from any radioactive background due to the limited beam intensity. However, with the available statistics, only an upper limit on the number of $2_1^+ \rightarrow 0_{gs}^+$ transitions in ^{100}Cd can be extracted. For this analysis all events within $E(2_1^+) = 1004 \pm 100$ keV in the Doppler corrected γ-ray spectrum in Fig. 6 are assigned to the projectile transition of interest. This energy region is defined from the maximum Doppler shift of the projectile γ-ray energy.

3. *Matrix elements and transitions in the targets*

The adopted value of the diagonal matrix element, $M_{22} = -0.42(8)\,e\,\mathrm{b}$, in ^{64}Zn [29] depends on the sign of the second-order interference term, $\langle 0_{gs}^+||E2||2_1^+\rangle \langle 2_1^+||E2||2_2^+\rangle \langle 0_{gs}^+||E2||2_2^+\rangle$. However, this ambiguity affects only the ^{102,104}Cd cross sections on the level of 3%, which

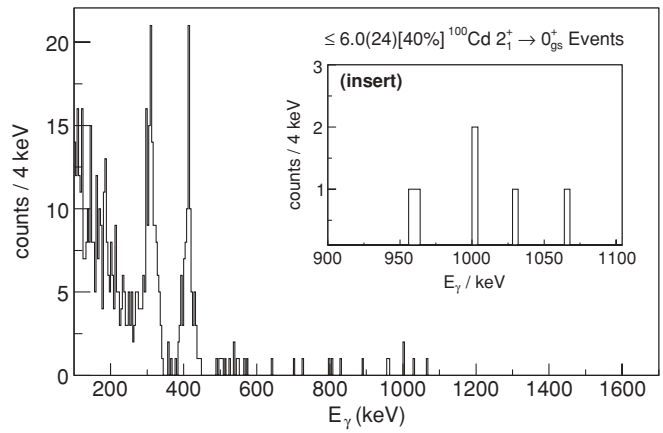

FIG. 6. Doppler-corrected γ-ray energy spectrum from the ^{100}Cd + ^{109}Ag measurement. All events present in the insert are assigned to the $2_1^+ \rightarrow 0_{gs}^+$ transition in ^{100}Cd. This leads to an upper limit of the corresponding $B(E2)$.

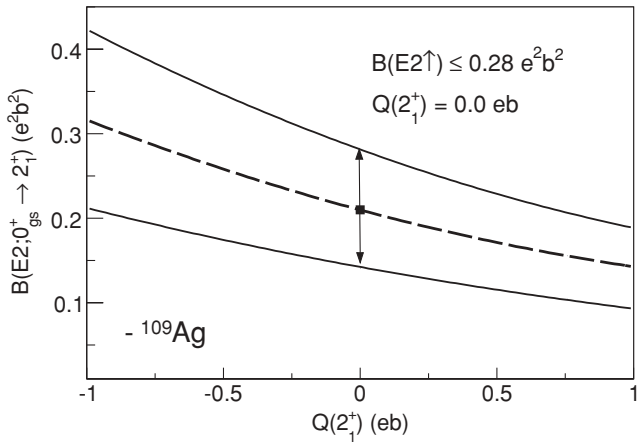

FIG. 7. The dashed line indicates the contour curve of the measured cross section of ^{100}Cd relative to ^{109}Ag. The $B(E2)$ value is extracted under the assumption that the $Q(2_1^+) = 0.0\,e$ b. This is in line with the observed experimental trend seen in the light Cd isotopes. The arrows indicate the extracted uncertainty.

is below the experimental precision. The positive interference term is used in this work due to its lower relative uncertainty.

In ^{109}Ag there exists an 8(1)% γ-decay branch from the 415.2 keV $5/2^-$ state to the 311.4 keV $3/2^-$ state [30]. This feeding of the 311.4 keV γ-ray yield is corrected for in the extraction of the Coulomb excitation cross sections when using ^{109}Ag as target.

V. RESULTS

In this section we present the contour curves, Fig. 7, Fig. 8(a), and Fig. 9(a), that result from the measured cross sections. The measurements relative to ^{64}Zn and ^{109}Ag are given by the black and red curves, respectively. The range of possible $B(E2)$ values is clearly limited by the ^{64}Zn cross section for small center-of-mass angles, $\theta_{\text{c.m.}}$, given by the blue curve in the same figure. The resulting likelihood distributions for ^{102,104}Cd are given in Fig. 8(b) and Fig. 9(b). The correlation between the static and dynamic moments is clear from these figures. The maximum likelihood estimator for the dynamic moments are $B(E2;\uparrow) = 0.33 \pm 0.01 \pm 0.02\,e^2\,\text{b}^2$ and $B(E2;\uparrow) = 0.28 \pm 0.02 \pm 0.02\,e^2\,\text{b}^2$ for ^{104}Cd and ^{102}Cd, respectively. The uncertainties are evaluated at the point of maximum likelihood in the (B, Q) plane. They are separated into statistical and systematic components. The primary source of the systematic error is the precision with which the $B(E2)$ values are known for the target isotopes. For ^{100}Cd a $B(E2) \leqslant 0.21 \pm 0.07\,e^2\,\text{b}^2$ is extracted for a $Q(2_1^+) = 0.0\,e$ b. The basis for this assumption is discussed further below. Note that the error in this case includes statistic and systematic effects. The results are summarized in Table V. A higher-lying second 2^+ state has not been observed experimentally in the present Cd isotopes. However, assuming that its energy is equal to that of the second 2^+ state in ^{106}Cd, a direct calculation shows that virtual quadrupole excitations via this state has an impact of <2% on the cross section. This will not affect the $B(E2)$ values. The resulting effect on the static quadrupole moments in the present Cd isotopes is <0.05 e b. Thus this systematic effect of a 2_2^+ state was not included in this work. In this investigation the $\langle 0_{\text{gs}}^+ || E2 || 2_2^+ \rangle$ and $\langle 2_1^+ || E2 || 2_2^+ \rangle$ matrix elements were taken from ^{106}Cd [35].

VI. SHELL-MODEL INTERPRETATION AND DISCUSSION

The first reorientation measurement was made in ^{114}Cd by J. de Boer *et al.* [36] and the finding of a large negative $Q(2_1^+)$ in that nucleus stimulated much discussion, see, e.g., Ref. [37–39] and references therein. One aim of the current work is to independently establish the trend of $B(E2)$ values for the light Cd isotopes using Coulomb excitation to compare this to the corresponding trend in the light Sn isotopes. The experimental trend of $B(E2)$ values in the Cd isotopic chain that results from this work shows a gradual, almost linear, increase starting with a $B(E2) = 0.28\,e^2\,\text{b}^2$ in ^{102}Cd toward a $B(E2) = 0.57\,e^2\,\text{b}^2$ in ^{118}Cd, see Fig. 10. The data on the neutron-rich side of stability remains scarce. The first measurements of the $B(E2)$ value have recently been carried out in ^{122,124}Cd [40] but the $Q(2_1^+)$ remains unknown in those isotopes. Current results seem to indicate a somewhat more rapid decrease in the $B(E2)$ values on the neutron-rich side. Still, it is not yet possible to draw a firm conclusion based

TABLE V. The experimental results obtained in this work as extracted from the maximum likelihood point. The uncertainties are statistical and systematical in origin. If only one uncertainty is quoted this corresponds to the total error. The second column indicates whether the lifetimes from Ref. [18] were included in the likelihood function. The correlation between the $B(E2)$ and the $Q(2_1^+)$ values is shown in Figs. 8(b) and 9(b).

Projectile	Incl. $\tau(2_1^+)$	$B(E2;0_{\text{gs}}^+ \to 2_1^+)$ $(e^2\,\text{b}^2)$	$Q(2_1^+)$ $(e\,\text{b})$	Target	Projectile σ_{E2} (mb)
^{104}Cd	No	$0.33 \pm 0.01 \pm 0.02$	$0.06 \pm 0.10 \pm 0.11$	^{64}Zn	307(39)
	Yes	0.39 ± 0.01	-0.52 ± 0.19	^{109}Ag	1013(61)
^{102}Cd	No	$0.28 \pm 0.02 \pm 0.02$	$0.22 \pm 0.11 \pm 0.15$	^{64}Zn	202(43)
	Yes	0.28 ± 0.04	0.20 ± 0.43	^{109}Ag	596(48)
^{100}Cd	No	$\leqslant 0.28$[a]	0.0[b]	^{109}Ag	201(64)

[a]The precision of this value is 33%.

[b]Fixed in the analysis to extract the corresponding $B(E2)$; see Fig. 7.

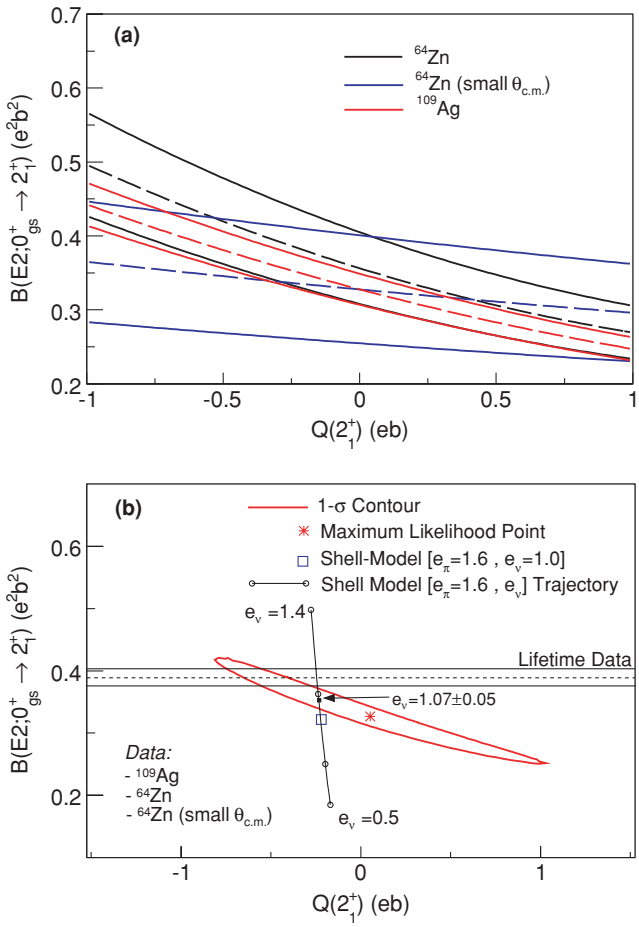

FIG. 8. (Color online) The final likelihood-interpreted results for ^{104}Cd based on the cross-section measurements presented here. (a) The contour curves in the $B(E2) - Q(2_1^+)$ plane for each measurement. The dashed curves indicate measured values and the solid curves the corresponding uncertainties. (b) The 1-σ contour of the likelihood function. The point of maximum likelihood is indicated with a red star together with horizontal and vertical lines for the corresponding uncertainty. The shell-model prediction with $e_\pi = 1.6\,e$ and $e_\nu = 1.0\,e$ for the location of the $B(E2\uparrow)$ and $Q(2_1^+)$ values is indicated with a blue square. The black curve marks the calculated trajectory of the $B(E2\uparrow)$ and $Q(2_1^+)$ values as a function of e_ν keeping $e_\pi = 1.6\,e$. The point of maximum likelihood along this trajectory gives the shell-model interpreted values presented in Table VI. The horizontal lines, marked with "Lifetime Data," indicate the $B(E2)$ value (dashed line) with uncertainties (solid lines) as extracted from the lifetime presented in Ref. [18].

on existing data for the neutron-rich isotopes. An interesting contrast between the Sn and Cd chains is that the apparent onset of collectivity observed in ^{106,108,110}Sn is not reproduced in an obvious way in ^{102,104,106}Cd. The reported high-precision measurement in Ref. [18] does indicate an increase in the $B(E2)$ value in ^{104}Cd but this appears not to be maintained for the lighter isotopes. However, this increase is not observed in our measurement.

In the following we discuss our results starting from a shell-model calculation based on a realistic interaction, i.e., without any phenomenological modifications, derived from a G-matrix-renormalized CD-Bonn nucleon-nucleon potential. This interaction reproduces fairly well the high spin states in ^{101,102}In and ^{99}Cd [6,7]. The nucleus ^{88}Sr is used as an inert core and the location of the single-particle energies were taken from Ref. [41]: $\varepsilon(\pi 1p_{1/2}) = 0.00$, $\varepsilon(\pi 0g_{9/2}) = 0.90$, $\varepsilon(\nu 1d_{5/2}) = 0.00$, $\varepsilon(\nu 2s_{1/2}) = 1.26$, $\varepsilon(\nu 1d_{3/2}) = 2.23$, $\varepsilon(\nu 0g_{7/2}) = 2.63$, and $\varepsilon(0h_{11/2}) = 3.50$ in units of MeV. The calculated $E(2_1^+)$ and $E(4_1^+)$ are almost identical to experimental values. Further, the theoretical $B(E2)$ and $Q(2_1^+)$ values for ^{106}Cd are well within the experimental uncertainties of the adopted values; see Table VI and Fig. 10.

One may now test the predictive power of the shell-model calculation using the probability distributions shown in Fig. 8(b) and Fig. 9(b). One approach to this issue is to keep either the proton effective charge (e_π) or the neutron effective charge (e_ν) constant while varying the other. For the present case the magnitude of the relevant diagonal and nondiagonal matrix elements results in a three times larger sensitivity of the predicted $B(E2)$ to a variation in e_ν compared to an equal variation in e_π. To facilitate a comparison with the light Sn isotopes it is primarily interesting to investigate renormalization effects in e_ν keeping e_π fixed. As a starting point one needs to select a pair of neutron and proton effective charges. The proton effective charge has been extracted from a previous lifetime measurement in ^{98}Cd [1]. However, a recent study [2] of a core-excited isomer in that nucleus indicates that systematic effects might have influenced the value of the extracted proton effective charge. Similarly new measurements of the de-excitation strength of the 6^+ isomer in ^{102}Sn [43] may lead to an improved neutron effective charge. Thus, awaiting further data for the lightest isotopes in the vicinity of ^{100}Sn we instead take ^{106}Cd as the starting point for our investigation. As can be seen in Fig. 10 the effective charges $e_\pi = 1.6\,e$ and $e_\nu = 1.0\,e$ reproduces the $B(E2)$ value in this nucleus. These values are also well in line with those used in previous calculations in this mass region [41,44,45]. The shell-model prediction for ^{102,104}Cd using these effective charges are indicated with squares in Fig. 8(b) and Fig. 9(b). For the ^{104}Cd case the prediction borders the 1-σ contour of the probability

TABLE VI. Shell-model interpretation (SM+exp) of the measured $B(E2; 0^+_{gs} \to 2^+_1)$ and $Q(2^+_1)$ values in units of $e^2\,b^2$ and $e\,b$, respectively. The energies of the first two excited states, $E(2^+_1)$ and $E(4^+_1)$, are also given in units of MeV. The effective proton and neutron charges of the shell-model (SM) values are $e_\pi = 1.6\,e$ and $e_\nu = 1.0$. See text for details.

	^{102}Cd	^{104}Cd	^{106}Cd
$E(2^+_1)_{SM}$	0.773	0.626	0.566
$E(2^+_1)_{exp}$	0.777	0.658	0.633
$E(4^+_1)_{SM}$	1.541	1.446	1.409
$E(4^+_1)_{exp}$	1.638	1.492	1.494
$B(E2)_{SM}$	0.24	0.32	0.38
$Q(2^+_1)_{SM}$	−0.18	−0.22	−0.24
$B(E2)_{SM+exp}$	0.32 ± 0.03	0.35 ± 0.02	0.384 ± 0.004[a]
$Q(2^+_1)_{SM+exp}$	-0.20 ± 0.01	-0.23 ± 0.01	-0.28 ± 0.08[a]

[a]Adopted experimental value, see Ref. [30].

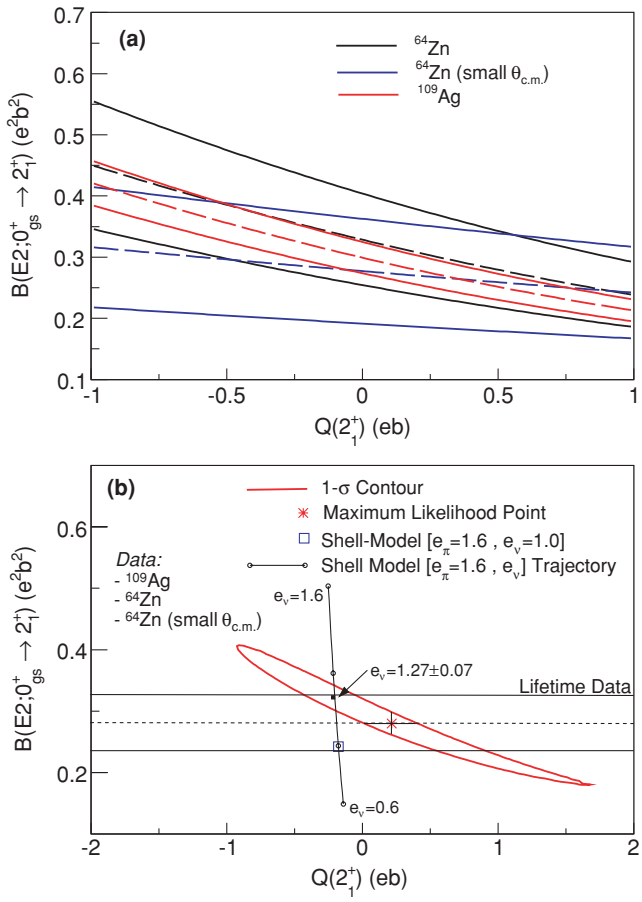

FIG. 9. (Color online) The final likelihood-interpreted results for ^{102}Cd based on the cross-section measurements presented here. The two plots (a) and (b) are identical to the ones shown for the ^{104}Cd case; see the caption of Fig. 8.

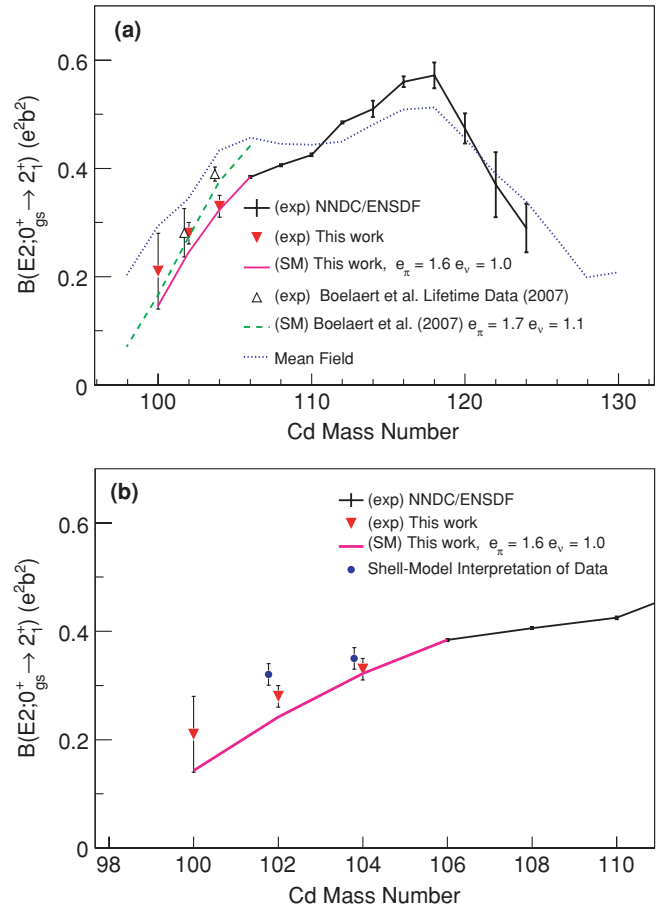

FIG. 10. (Color online) (a) Experimental and theoretical $B(E2;0^+_{gs} \rightarrow 2^+_1)$ and values in the Cd isotopes. The "REX-ISOLDE" values (red triangles) are the maximum likelihood estimators extracted in this work. The Boelaert *et al.* lifetime data is Ref. [18], the Boelaert *et al.* shell-model calculation is Ref. [11], and the mean-field calculation is Ref. [42]. (b) Same figure expanded around the neutron-deficient region. The blue dots represent the $B(E2)$ values obtained using the shell-model interpretation of the measured data. See text for details.

distribution while for the ^{102}Cd case the deviation is larger. A variation of e_ν will trace out a trajectory in the (B, Q) plane. The point of maximum likelihood along this trajectory gives the neutron effective charge that reproduces the experimental result with highest probability within the model. Consequently, tracing this trajectory, keeping $e_\pi = 1.6\,e$ fixed, gives a direct measure of the renormalization required for the shell-model to reproduce the data in ^{102,104}Cd. For ^{104}Cd the maximum likelihood is reached for $e_\nu = 1.07 \pm 0.05$ while for ^{102}Cd the corresponding number is $e_\nu = 1.27 \pm 0.07$. Thus, for the latter case the renormalization of the neutron effective charge amounts to 27% within 3σ. Repeating this investigation with the proton effective charges $e_\pi = 1.4$ and $e_\pi = 1.8\,e$ requires $e_\nu = 1.07\,e$ and $e_\nu = 0.93\,e$ to reproduce the experimental $B(E2)$ value in ^{106}Cd. For ^{102}Cd the maximum likelihood is then reached for $e_\nu = 1.37 \pm 0.07\,e$ and $e_\nu = 1.17 \pm 0.07\,e$. In total, this investigation indicates a ~25% renormalization of the neutron effective charge when moving from ^{106}Cd to ^{102}Cd. The corresponding $B(E2)$ values extracted with maximum likelihood are given in Table VI and with blue dots in Fig. 10(b). It is interesting to note that the predicted $Q(2_1^+)$ are limited to a very narrow range. It is therefore clear from the picture that the presented values are close to the ones that would be obtained from an interpretation based on a fix $Q(2_1^+)$ value from the shell-model. In conclusion, a renormalization of the neutron effective charge in the light Cd isotopes appears necessary although the effect on the observed $B(E2)$ values is not as conspicuous as suggested in the light Sn isotopes [13–16].

It should be mentioned that theoretical predictions for the light Cd isotopes have also been presented in two recent works [11,42]. The shell-model calculations in Ref. [11] were carried out with a valence space consisting of the proton $\pi(1p_{1/2}, 0g_{9/2})$ and neutron $\nu(1d_{5/2}, 2s_{1/2}, 1d_{3/2}, 0g_{7/2}, 0h_{11/2})$ orbits outside an inert $^{88}_{38}$Sr$_{50}$ core. For further details see Ref. [11]. The results from this calculation are shown in Fig. 10 where the results from a beyond mean-field calculation [42] using the Gogny force is also plotted. Earlier theoretical models [12] of the neutron-deficient Cd isotopes include taking ^{100}Sn as a core and using a neutron-proton interaction of quadrupole-quadrupole type.

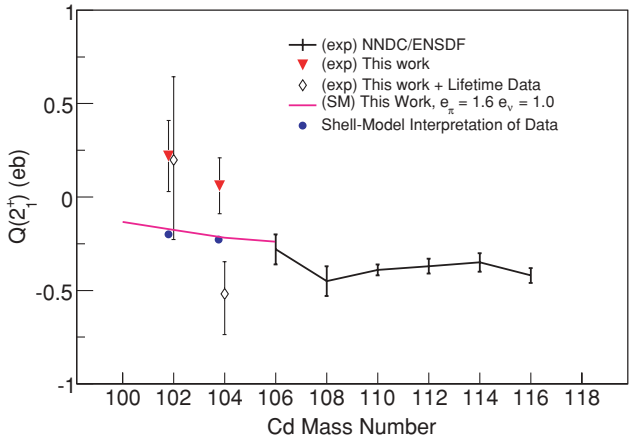

FIG. 11. (Color online) The experimentally known $Q(2_1^+)$ values in the even-mass Cd isotopes. The results of the shell-model calculation carried out in this work are indicated with a magenta line. Invoking the previously published lifetime data [18] in the likelihood function gives the $Q(2_1^+)$ values marked with diamonds. The numerical values for these are given in Table V. See text for details.

As can be seen in Fig. 11 the experimental $Q(2_1^+)$ in ^{104}Cd is lower than that in ^{106}Cd when invoking the previously published lifetime data [18]. While the value from our likelihood analysis lies closer to zero for ^{104}Cd and also somewhat closer to the shell-model prediction the values extracted using both methods almost identical for ^{102}Cd. This may be a further indication of a slightly too-large $B(E2)$ value extracted from the lifetime measurement in Ref. [18]. The shell-model calculation also indicates a $Q(2_1^+) \approx 0\,e\,$b in ^{100}Cd and therefore strengthens the grounds on which the $B(E2)$ value in ^{100}Cd is extracted.

In a spherical harmonic vibrator model the static quadrupole moment is also predicted to be identical to zero [46]. In a article by Alaga [47], the particle-vibrator model was shown to give a $Q(2_1^+) = -0.33\,$b for the Cd isotopes in the midshell region, which is in agreement with the later adopted experimental value, see Fig. 11 and Refs. [37,38]. Within that model the quadrupole moment in vibration-like nuclei is a consequence of the interaction between the proton degree of freedom and the vibrator here given by the neutrons. Moreover, energy-weighted sum-rule calculations [48] and investigations [49] using the interacting boson approximation are in agreement with the experimental $Q(2_1^+)$ values in $^{106-116}$Cd.

Evidently, experimental transition probabilities in the two proton-hole, $N = 50$, nucleus ^{98}Cd are of importance in the investigation of the nucleon-nucleon interaction in the ^{100}Sn region. Expanded theoretical investigations and shell-model calculations relating to this question have been initiated [50].

ACKNOWLEDGMENTS

This work was supported by the Swedish Research Council, the German Federal Ministry of Education and Research under Grant 06KY205I, and the European Union under Contract RII3-EURONS 506065.

[1] M. Górska *et al.*, Phys. Rev. Lett. **79**, 2415 (1997).
[2] A. Blazhev *et al.*, Phys. Rev. C **69**, 064304 (2004).
[3] N. Redon, J. Meyer, M. Meyer, P. Quentin, P. Bonche, H. Flocard, and P. H. Heenen, Phys. Rev. C **38**, 550 (1988).
[4] K. Heyde, P. Van Isacker, M. Waroquier, G. Wenes, and M. Sambataro, Phys. Rev. C **25**, 3160 (1982).
[5] A. Pandoh, R. Devi, and S. K. Khosa, Phys. Rev. C **60**, 047302 (1999).
[6] M. Lipoglavsek *et al.*, Phys. Rev. C **65**, 021302(R) (2002).
[7] M. Lipoglavsek *et al.*, Phys. Rev. C **66**, 011302(R) (2002).
[8] J. Persson *et al.*, Nucl. Phys. **A627**, 101 (1997).
[9] M. Palacz *et al.*, Nucl. Phys. **A624**, 210 (1997).
[10] M. Palacz *et al.*, Nucl. Phys. **A608**, 227 (1996).
[11] N. Boelaert, N. Smirnova, K. Heyde, and J. Jolie, Phys. Rev. C **75**, 014316 (2007).
[12] J. Sau *et al.*, Nucl. Phys. **A410**, 14 (1983).
[13] A. Banu *et al.*, Phys. Rev. C **72**, 061305(R) (2005).
[14] C. Vaman *et al.*, Phys. Rev. Lett. **99**, 162501 (2007).
[15] J. Cederkäll *et al.*, Phys. Rev. Lett. **98**, 172501 (2007).
[16] A. Ekström *et al.*, Phys. Rev. Lett. **101**, 012502 (2008).
[17] G. Müller *et al.*, Phys. Rev. C **64**, 014305 (2001).
[18] N. Boelaert *et al.*, Phys. Rev. C **75**, 054311 (2007).
[19] K. Alder and A. Winther, *Electromagnetic Excitation* (North-Holland, Amsterdam, 1975).
[20] G. Breit *et al.*, Phys. Rev. **103**, 727 (1956).
[21] J. V. de Walle *et al.*, Phys. Rev. C **79**, 014309 (2009).
[22] U. Köster *et al.*, Nucl. Instrum. Methods B **266**, 4229 (2008).
[23] F. Wenander, Nucl. Phys. **A701**, 528 (2002).
[24] A. N. Ostrowski *et al.*, Nucl. Instrum. Methods A **480**, 448 (2002).
[25] J. F. Ziegler, Nucl. Instrum. Methods B **219-220**, 1027 (2004)
[26] N. Bree *et al.*, Phys. Rev. C **78**, 047301 (2008).
[27] S. Raman *et al.*, At. Data Nucl. Data Tables **78**, 1 (2001).
[28] N. Stone, At. Data Nucl. Data Tables **90**, 75 (2005).
[29] S. Salém-Vasconcelos, M. J. Bechara, J. H. Hirata, and O. Dietzsch, Phys. Rev. C **38**, 2439 (1988).
[30] ENSDF, http://www.nndc.bnl.gov/ensdf/.
[31] P. Raghavan, At. Data Nucl. Data Tables **42**, 189 (1989).
[32] M. J. Throop *et al.*, Phys. Lett. **B41**, 585 (1972).
[33] J. Ljungvall *et al.*, Phys. Rev. Lett. **100**, 102502 (2008).
[34] H. Ower, computer code CLX.
[35] W. Milner *et al.*, Nucl. Phys. **A129**, 687 (1969).
[36] J. de Boer *et al.*, Phys. Rev. Lett. **14**, 564 (1965).
[37] M. T. Esat *et al.*, Phys. Lett. **B61**, 242 (1976).
[38] M. T. Esat *et al.*, Nucl. Phys. **A274**, 237 (1976).
[39] C. Fahlander *et al.*, Nucl. Phys. **A485**, 327 (1988).
[40] T. Kröll *et al.*, AIP Conf. Proc. **831**, 119 (2006).
[41] A. Holt, T. Engeland, M. Hjorth-Jensen, and E. Osnes, Phys. Rev. C **61**, 064318 (2000).
[42] T. R. Rodriguez *et al.*, Phys. Lett. **B668**, 410 (2008).
[43] M. Górska (private communication).
[44] B. A. Brown *et al.*, Phys. Rev. C **13**, 1900 (1976).

[45] K. Sieja, F. Nowacki, K. Langanke, and G. Martinez-Pinedo, Phys. Rev. C **79**, 064310 (2009).
[46] Aa. Bohr and B. Mottelson, *Nuclear Structure* (Benjamin, New York, 1969), Vol. II.
[47] G. Alaga *et al.*, Phys. Lett. **B43**, 459 (1973).
[48] W. Koo *et al.*, Nucl. Phys. **A315**, 21 (1979).
[49] I. Morrison *et al.*, Nucl. Phys. **A350**, 89 (1980).
[50] A. Ekström *et al.* (to be published).